

RESEARCH ARTICLE

10.1002/2013JD021303

Key Points:

- A retrieval for snow microphysical properties is characterized
- Ground observations provide information about size-dependent snow properties
- Information content metrics suggest improvements for future observing systems

Correspondence to:

N. B. Wood,
norman.wood@ssec.wisc.edu

Citation:

Wood, N. B., T. S. L'Ecuyer, A. J. Heymsfield, G. L. Stephens, D. R. Hudak, and P. Rodriguez (2014), Estimating snow microphysical properties using collocated multisensor observations, *J. Geophys. Res. Atmos.*, 119, 8941–8961, doi:10.1002/2013JD021303.

Received 16 DEC 2013

Accepted 21 JUN 2014

Accepted article online 26 JUN 2014

Published online 21 JUL 2014

Estimating snow microphysical properties using collocated multisensor observations

Norman B. Wood¹, Tristan S. L'Ecuyer², Andrew J. Heymsfield³, Graeme L. Stephens⁴, David R. Hudak⁵, and Peter Rodriguez⁵
¹Cooperative Institute for Meteorological Satellite Studies, University of Wisconsin–Madison, Madison, Wisconsin, USA,

²Department of Atmospheric and Oceanic Sciences, University of Wisconsin–Madison, Madison, Wisconsin, USA,

³National Center for Atmospheric Research, Boulder, Colorado, USA, ⁴Jet Propulsion Laboratory, National Aeronautics and Space Administration, Pasadena, California, USA, ⁵Cloud Physics and Severe Weather Research Section, Environment Canada, King City, Ontario, Canada

Abstract The ability of ground-based in situ and remote sensing observations to constrain microphysical properties for dry snow is examined using a Bayesian optimal estimation retrieval method. Power functions describing the variation of mass and horizontally projected area with particle size and a parameter related to particle shape are retrieved from near-Rayleigh radar reflectivity, particle size distribution, snowfall rate, and size-resolved particle fall speeds. Algorithm performance is explored in the context of instruments deployed during the Canadian CloudSat CALIPSO Validation Project, but the algorithm is adaptable to other similar combinations of sensors. Critical estimates of observational and forward model uncertainties are developed and used to quantify the performance of the method using synthetic cases developed from actual observations of snow events. In addition to illustrating the technique, the results demonstrate that this combination of sensors provides useful constraints on the mass parameters and on the coefficient of the area power function but only weakly constrains the exponent of the area power function and the shape parameter. Information content metrics show that about two independent quantities are measured by the suite of observations and that the method is able to resolve about eight distinct realizations of the state vector containing the mass and area power function parameters. Alternate assumptions about observational and forward model uncertainties reveal that improved modeling of particle fall speeds could contribute substantial improvements to the performance of the method.

1. Introduction

Knowledge of snow microphysical properties is essential for the remote sensing of snowfall using space- or ground-based radar observations. A primary difficulty in such remote sensing problems is the nonunique relationship between radar reflectivity and snowfall rate, a relationship determined by the unknown microphysical properties of the observed snow. With even the simplest of representations for these properties, the number of unknown microphysical parameters associated with a single radar bin results in a significantly underconstrained problem.

Prior information may be used to address such an underconstrained problem. Potentially useful a priori microphysical information includes descriptions of snow particle mass and horizontally projected area as functions of particle size, so-called $m - D$ and $A - D$ relationships. These relationships have often been expressed using power functions in studies of particles observed at the surface, particularly for mass. Nakaya and Terada [1935] developed $m - D$ power functions with integer exponents for six broadly defined particle habits. More recent studies have reported $m - D$ power functions explicitly [e.g., Locatelli and Hobbs, 1974; Zikmunda and Vali, 1972, 1977; Mitchell et al., 1990] or implicitly via parameterizations of particle density as a function of size [Magono and Nakamura, 1995; Heymsfield, 1972]. The development of $A - D$ power functions has been somewhat less common. Davis [1974] used crystal images and dimensional data from earlier ground-based studies to produce $A - D$ power functions, again for various habits. Heymsfield and Miloshevich [2003] used ground- and aircraft-based observations from multiple sources to form power functions for area ratio, which are simply transformable to give area. Mitchell [1996] evaluated and compiled $m - D$ and $A - D$ relationships from much of the literature available at the time.

Determining the parameters of these functions has typically involved analysis of single-particle observations [e.g., *Kajikawa, 1972; Locatelli and Hobbs, 1974; Mitchell et al., 1990*] or, for mass, bulk approaches in which particle size distributions are observed and related to an integral property of the distribution like accumulated precipitation or radar reflectivity [e.g., *Brandes et al., 2007*]. Few such studies evaluated mass and area properties simultaneously, so physical consistency between area and mass parameters has not been assured. As a result, information regarding covariances between parameters, which can be an important retrieval constraint, has been lacking. Especially for the single-particle studies, sample sizes have been small and the studies have been performed primarily in mountain locations, limiting the characterization of the uncertainties and the environmental variability for the estimated parameters.

This work examines a novel application of the optimal estimation retrieval method [*Rodgers, 2000*] that estimates dry snow microphysical properties using intensive ground-based observations of snowfall. Observations of snowfall rate, snow particle size distribution, size-resolved fall speeds, and 9.35 GHz (X-band) radar reflectivity are used to estimate the parameters of power functions describing particle mass and horizontally projected area as functions of particle size. The retrieval results are expressed in terms of probability density functions (PDFs) that define the expected values and uncertainties for these parameters. This work tests the retrieval using synthetic cases constructed using observations from a snow measurement field campaign, then characterizes the performance of the observing system using information content metrics. Although several studies have suggested power functions with size-varying parameters [e.g., *Mitchell, 1996; Matrosov, 2007*], this work uses power functions whose parameters are invariant with size to construct the synthetic test cases and to define the retrieved state. Doing so provides a fundamental test of retrieval performance and establishes a basis for future work in which the synthetic cases or retrieved state is described using more complex relationships. Section 2 reviews the optimal estimation method and provides the physical basis for the retrieval. Section 3 describes the microphysical quantities to be retrieved and the a priori knowledge of their distribution. Section 4 defines the observation vector used by the retrieval and the synthetic cases used to test the retrieval performance. The forward model and the uncertainties it contributes to the retrieval process are quantified in section 5. Finally, retrieval performance is characterized in terms of several different information content metrics in section 6.

2. Retrieval Method

Several recent field experiments focusing wholly or in part on cold season precipitation (the Canadian CloudSat/CALIPSO Validation Project, C3VP [*Hudak et al., 2006a*], the Light Precipitation Validation Experiment [*Petersen et al., 2011*], and the Global Precipitation Mission Cold-Season Precipitation Experiment [*Hudak et al., 2012*]) operated highly instrumented ground stations for measuring precipitation. The measurements provided by these stations have included near-Rayleigh radar reflectivity, particle size distributions, size-resolved particle fall speeds, and precipitation rates. At its primary ground facility, for example, C3VP deployed the McGill University Vertically Pointing X-band Doppler Radar (VertiX) [*Fabry and Zawadzki, 1995*], the National Aeronautics and Space Administration's Snow Video Imager (SVI) [*Newman et al., 2009*], Colorado State University's 2-D Video Disdrometer (2DVD) [*Thurai and Bringi, 2005*], and a Vaisala FD12P [*Vaisala, 2002*] supplemented with other precipitation measurements. Figure 1 shows typical observations, less 2DVD fall speeds, for a C3VP lake effect snow event on 28 January 2007.

These measurements depend on the underlying microphysical properties of the observed snow. The measured quantities are not fully independent, and the relationships between the microphysical properties and the measurements are complex. Even with simple representations of the microphysical properties, in most cases such a suite of measurements does not fully constrain the microphysics, and so a priori assumptions are required to make the retrieval problem tractable.

Optimal estimation (OE) [*Rodgers, 2000*] provides a method to estimate these underlying microphysical properties and to incorporate a priori constraints. OE employs an explicit forward model that defines a functional relationship between the observations \mathbf{y} and the quantities to be retrieved, or state variables, \mathbf{x} . The forward model $\mathbf{F}(\mathbf{x}, \tilde{\mathbf{b}})$ gives an approximation of the true physical relationship between \mathbf{x} and \mathbf{y} ; thus, there are uncertainties associated with both the observations \mathbf{y} and the forward modeled quantities \mathbf{F} . Allowing for these uncertainties gives the statement of the forward problem:

$$\mathbf{y} = \mathbf{F}(\mathbf{x}, \tilde{\mathbf{b}}) + \epsilon, \quad (1)$$

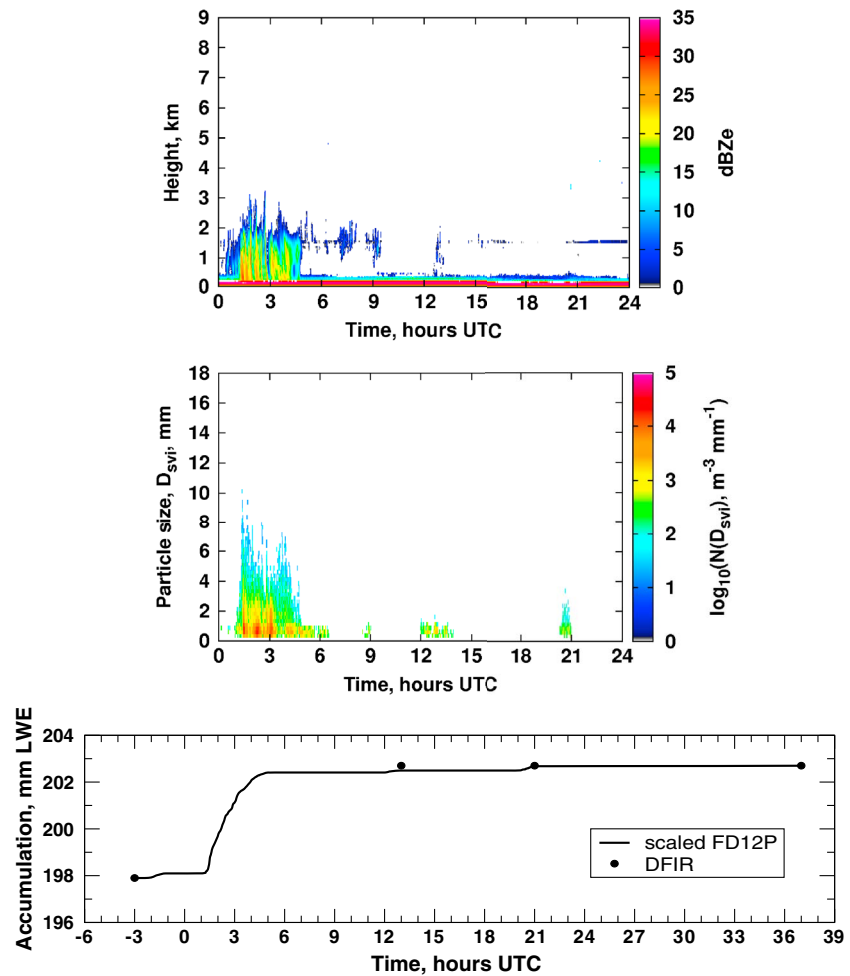


Figure 1. (top) VertiX, (middle) SVI, and (bottom) FD12P observations for the 28 January 2007 snowfall event.

where ϵ represents the total uncertainty, due both to measurement uncertainty and to uncertainties in the forward model, and $\tilde{\mathbf{b}}$ are other influence parameters, not to be retrieved, where the tilde indicates that these parameters may be known imperfectly.

To find the retrieved estimate $\hat{\mathbf{x}}$ of the state, the cost function

$$\Phi(\mathbf{x}, \mathbf{y}, \mathbf{x}_a) = (\mathbf{y} - \mathbf{F}(\mathbf{x}, \tilde{\mathbf{b}}))^T \mathbf{S}_\epsilon^{-1} (\mathbf{y} - \mathbf{F}(\mathbf{x}, \tilde{\mathbf{b}})) + (\mathbf{x} - \mathbf{x}_a)^T \mathbf{S}_a^{-1} (\mathbf{x} - \mathbf{x}_a) \quad (2)$$

is minimized with respect to \mathbf{x} [Rodgers, 2000]. The cost function incorporates prior information about the state vector in the form of expected values \mathbf{x}_a and their covariances \mathbf{S}_a .

The covariance matrix \mathbf{S}_ϵ represents the combined measurement and forward model uncertainties. The total error ϵ (1) includes contributions from measurement uncertainty, forward model errors, and uncertain influence parameters [Rodgers, 2000]:

$$\epsilon = \epsilon_y + \Delta \mathbf{F}(\mathbf{x}, \mathbf{b}) + \frac{\partial \mathbf{F}}{\partial \mathbf{b}} (\mathbf{b} - \tilde{\mathbf{b}}). \quad (3)$$

In principle, these errors may consist of both systematic biases and random components, but the retrieval approach assumes that recognized biases have been corrected to the extent possible and characterizes residual random errors by the covariance matrix \mathbf{S}_ϵ

$$\mathbf{S}_\epsilon = \mathbf{S}_y + \mathbf{S}_F + \mathbf{S}_B, \quad (4)$$

where \mathbf{S}_y , \mathbf{S}_F , and \mathbf{S}_B represent measurement, forward model, and influence parameter error covariance matrices, respectively. Diagonal elements in \mathbf{S}_e represent variances due to measurement noise, forward model uncertainties, and variability in all prescribed influence parameters while off-diagonal elements represent correlations between these quantities.

Provided that the forward model is not excessively nonlinear, the vector $\hat{\mathbf{x}}$ can be found by Newtonian iteration:

$$\hat{\mathbf{x}}_{i+1} = \hat{\mathbf{x}}_i + (\mathbf{S}_a^{-1} + \mathbf{K}_i^T \mathbf{S}_e^{-1} \mathbf{K}_i)^{-1} \cdot [\mathbf{K}_i^T \mathbf{S}_e^{-1} (\mathbf{y} - \mathbf{F}(\hat{\mathbf{x}}_i, \tilde{\mathbf{b}})) - \mathbf{S}_a^{-1} (\hat{\mathbf{x}}_i - \mathbf{x}_a)], \quad (5)$$

where \mathbf{K} is the Jacobian of the forward model with respect to the state vector and $\mathbf{K}_i = \mathbf{K}(\hat{\mathbf{x}}_i)$. At convergence, the solution $\hat{\mathbf{x}}$ is obtained and its covariance matrix $\hat{\mathbf{S}}_x$ is calculated as

$$\hat{\mathbf{S}}_x = (\hat{\mathbf{K}}^T \mathbf{S}_e^{-1} \hat{\mathbf{K}} + \mathbf{S}_a^{-1})^{-1}, \quad (6)$$

where $\hat{\mathbf{K}}$ is the forward model Jacobian evaluated at the retrieved state and $\hat{\mathbf{x}}$ and $\hat{\mathbf{S}}_x$ describe a multivariate normal distribution. Strong nonlinearity may cause nonconvergence or convergence to a spurious state. To test for spurious convergence, a chi-square parameter is calculated from the final state. A value less than the number of measurements indicates reasonable convergence [Rodgers, 2000].

This approach presupposes that the model-measurement uncertainties and the a priori distribution of the state variables are described by multivariate normal distributions. Lack of detailed knowledge of the uncertainties and the a priori state may make this supposition questionable; however, considering continuous distributions with constrained widths, the normal, or Gaussian, form maximizes the entropy of the distribution [Rodgers, 2000; Shannon and Weaver, 1949], so assuming the normal form introduces the minimum possible information about the uncertainties and the prior state. To choose otherwise would introduce additional constraints on the retrieval which are generally not justified.

2.1. Retrieval Performance Metrics

Several metrics which provide quantitative information about the performance of the retrieval can be determined from the optimal estimation results.

The Shannon Information Content, H , measures the reduction of uncertainty in the retrieved state in comparison to the a priori uncertainty [Rodgers, 2000]:

$$H = \frac{1}{2} \log_2 |\mathbf{S}_a \hat{\mathbf{S}}_x^{-1}|. \quad (7)$$

H quantifies differences in the entropies [Shannon and Weaver, 1949] of the distributions described by \mathbf{S}_a and $\hat{\mathbf{S}}_x$. Rodgers [2000] interprets H in terms of changes in the volume enclosed by a surface of constant probability, and L'Ecuyer et al. [2006] further characterize H as a measure of the resolution of the observing system. When expressed using base-2 logarithms, H then gives the binary bits of resolution provided by the measurements, suggesting the measurements can resolve 2^H states within the a priori state space.

The degrees of freedom for signal, d_s , describes the number of independent quantities provided by the measurements which are significant compared to the combined forward model and measurement uncertainties. The degrees of freedom for signal can be shown to be equal to the trace of the \mathbf{A} matrix [Rodgers, 2000].

The averaging kernel matrix, or \mathbf{A} matrix, is given by

$$\mathbf{A} = (\hat{\mathbf{K}}^T \mathbf{S}_e^{-1} \hat{\mathbf{K}} + \mathbf{S}_a^{-1})^{-1} \hat{\mathbf{K}}^T \mathbf{S}_e^{-1} \hat{\mathbf{K}}. \quad (8)$$

The nearer \mathbf{A} is to diagonal, the more directly a particular element of $\hat{\mathbf{x}}$ is determined by its particular true state and a priori value. Diagonal values near 1.0 indicate that the retrieved value is determined more completely by the true state rather than the a priori.

2.2. Physical Basis

Typical measurements, including radar reflectivity, size-resolved fall speeds, and snowfall rate, were introduced in section 2. Provided the radar wavelength is such that scattering by snow particles follows the Rayleigh approximation for spheres, *Atlas et al.* [1953] showed that low-density, irregularly shaped dry snow particles can be treated as equal volume ice spheres to calculate radar scattering properties with small error. For the short path lengths and observing conditions applicable to these observations, attenuation by gases and snow particles should be negligible [Matrosov, 1998]. Reflectivity for the Rayleigh sphere approximation can then be written as [e.g., Wood et al., 2013]

$$Ze = \frac{36}{\pi^2 \rho_{ice}^2} \frac{\|K_i\|^2}{\|K_w\|^2} \int_{D_{M,min}}^{D_{M,max}} N(D_M) [m(D_M)]^2 dD_M, \quad (9)$$

where D_M is the particle maximum dimension, $m(D_M)$ is the size-varying particle mass, ρ_{ice} is the density of solid ice, $K_w = (n_{liq}^2 - 1)/(n_{liq}^2 + 2)$ where n_{liq} is the complex refractive index of liquid water, $K_i = (n_{ice}^2 - 1)/(n_{ice}^2 + 2)$ where n_{ice} is the complex refractive index of ice, and $N(D_M)$ is the particle size distribution.

While snow particle size may be measured several different ways (e.g., melted diameter and equivalent area diameter), D_M is more closely related to the sizes measured by optical disdrometers and aircraft 2-D probes than other measures. Additionally, explicit physical models for fall speed depend on a particle dimension which is typically taken to be D_M [Mitchell and Heymsfield, 2005].

The fall speed relationship developed by Mitchell and Heymsfield (hereafter MH05) is physically based and intended to accommodate larger particles like aggregates. The Reynolds number Re is

$$Re(D_M) = \frac{\delta_0^2}{4} \left[\left(1 + \frac{4\sqrt{X(D_M)}}{\delta_0^2 \sqrt{C_0}} \right)^{1/2} - 1 \right]^2 - a_0 [X(D_M)]^{b_0}, \quad (10)$$

with parameters $a_0 = 0.0017$ and $b_0 = 0.8$; δ_0 is a unitless constant related to boundary layer thickness and C_0 is the limiting drag coefficient under conditions dominated by pressure drag. Bohm [1989] estimated values of $C_0 = 0.6$ and $\delta_0 = 5.83$. $X(D_M)$ is a dimensionless group which is often identified as the Best or Davies number in atmospheric science literature [e.g., List and Schemenauer, 1971; Bohm, 1989; Mitchell, 1996] but which is equivalent to the Archimedes number used to characterize the ratio of gravitational to viscous forces acting on a particle or fluid parcel embedded in a fluid [Mory, 2011]. For nonspherical particles with buoyancy force ignored, the Best number is expressed in terms of $m(D_M)$ and $A_p(D_M)$ as [Mitchell, 1996]

$$X(D_M) = C_d Re^2 = \frac{2D_M^2 \rho_a g}{\mu^2} \frac{m(D_M)}{A_p(D_M)}, \quad (11)$$

where C_d is the drag coefficient, $A_p(D_M)$ is the size-varying particle horizontally projected area, ρ_a is the air density, μ is the viscosity, and g is gravitational acceleration. Obtaining Re from (10), the fall speed can be found from

$$V(D_M) = \frac{Re(D_M)\mu}{\rho_a D_M}. \quad (12)$$

Fall speed depends explicitly on particle size D_M , the particle mass, the projected area, air density, and air viscosity, as well as the parameters δ_0 , C_0 , a_0 , and b_0 . Treating air as an ideal gas allows density and viscosity to be calculated from air temperature T and pressure p via Sutherland's formula [Sutherland, 1893].

Snowfall rates are expressed using the size distribution, particle masses, and particle fall speeds $V(D_M)$ as

$$P = \frac{1}{\rho_{liq}} \int_{D_{M,min}}^{D_{M,max}} N(D_M) m(D_M) V(D_M) dD_M \quad (13)$$

where P is in units of liquid water depth per unit time (e.g., mm h⁻¹) and ρ_{liq} is liquid water density.

Table 1. Estimates of the A Priori State for the C3VP Microphysics Retrieval^a

	Mean	Correlation	Variance	Covariance
$\ln(\alpha)$	-6.181	0.753	2.474	0.585
β	2.067		0.244	
$\ln(\gamma)$	-1.556	0.836	0.392	0.118
σ	1.785		0.0507	

^aValues are appropriate for cgs units.

3. The State Vector

The preceding relationships show that, given measurements of the particle size distribution, these observations provide information about the size-dependent masses, $m(D_M)$, and horizontally projected areas, $A_p(D_M)$, of snowfall. These properties are often described using power functions of the particle maximum dimension [e.g., Mitchell, 1996]

$$m(D_M) = \alpha D_M^\beta, \quad (14)$$

$$A_p(D_M) = \gamma D_M^\sigma. \quad (15)$$

The microphysical parameters to be retrieved, then, are the coefficients and exponents of the power functions for mass and horizontally projected area.

Values for α and γ are expected to range over 2 or more orders of magnitude, so these variables are log transformed. In practice, the masses and areas calculated by these functions are capped to be no larger than the mass of a solid ice sphere and the area of a circle of a given particle size. For the values reported here, cgs units are used. With D_M in centimeters, units for α and γ are such that m is given in grams and A_p in square centimeters.

Particle sizes observed by imaging disdrometers are not equal to D_M due to the effects of particle orientation and viewing geometry. Disdrometer size distributions, then, are not based on D_M but rather on some observed particle size D_{obs} . Wood *et al.* [2013] introduced a parameter ϕ to convert observed size distributions into distributions based on D_M . Since ϕ may vary significantly depending on the disdrometer and snow particle shape, it is added to the state vector to be retrieved, giving

$$\mathbf{x} = [\ln(\alpha) \ \beta \ \ln(\gamma) \ \sigma \ \phi]^T. \quad (16)$$

3.1. A Priori Estimates of the State Vector Distribution

Prior information about the distribution of values for the state vector is introduced through the mean and covariance matrix of a multivariate normally distributed a priori PDF defined by \mathbf{x}_a and \mathbf{S}_a . Prior values of $\ln(\alpha)$, β , $\ln(\gamma)$, and σ , their variances, and covariances were estimated using the results from prior studies of snow microphysical properties and results from a new analysis [Wood, 2011] of snow particle observations originally made by Kajikawa [Kajikawa, 1972, 1975, 1982]. Mass-dimension parameters are taken from Zikmunda and Vali [1972], Locatelli and Hobbs [1974], and Mitchell *et al.* [1990], and the independent relationships from Mitchell [1996]. Area-dimension parameters include results from Heymsfield [1972], Mitchell [1996], and Heymsfield and Miloshevich [2003], omitting those from the latter study pertaining to the Kajikawa observations to avoid duplication.

The estimated parameters from these studies were treated as samples drawn from the environmental distribution of the state vector, \mathbf{x} , and expected values of $\ln(\alpha)$, β , $\ln(\gamma)$, and σ were calculated along with their variances and covariances [Wood, 2011]. Although some information regarding snowflake geometry or habit might have been used from the prior studies to construct habit-dependent a priori PDFs, this habit information will likely be lacking in typical remote sensing observations. Therefore, all prior observations were combined to construct a habit-independent a priori PDF. Because studies from which simultaneously estimated mass- and area-dimension power function parameters can be determined are lacking (the Kajikawa observations are a rare exception), covariances between $\ln(\alpha)$ and $\ln(\gamma)$, $\ln(\alpha)$ and σ , β and $\ln(\gamma)$, and β and σ were omitted (Table 1).

The resulting distribution depends on the frequencies of occurrence of various particle types in the sample. The number of studies supplying these data is small and, for studies using ground-based observations, the study sites were often in mountainous locations. As a result, the sample may not accurately represent the frequencies of occurrence in the environment, and the properties for a given particle type may also not be representative of particles found in the broader environment. Further, the parameters provided by these

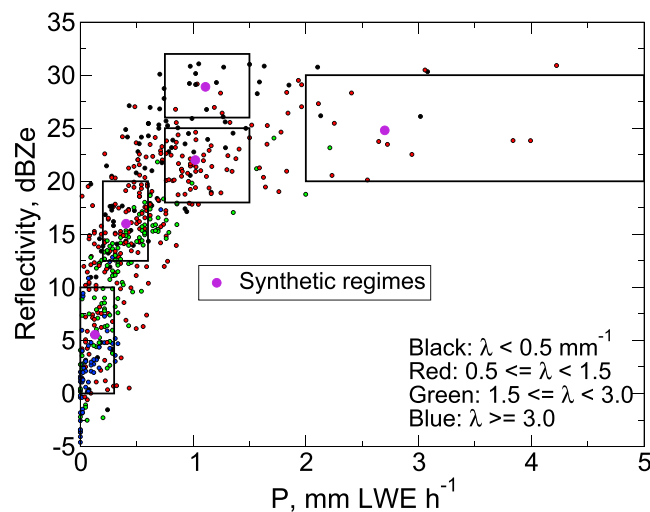


Figure 2. VertiX reflectivities versus FD12P snowfall rates from the 5 min average C3VP observations. VertiX reflectivities have been corrected to ground level, and snowfall rates have been scaled to match double fence intercomparison reference (DFIR) accumulations. Dot colors indicate the slope of an exponential distribution fitted to the observed size distribution. Boxes indicate boundaries used to define snowfall regimes, and large dots show averaged reflectivities and snowfall rates for each regime.

modeling described in Wood *et al.* [2013] as 0.825 and 0.125². The value 0.825 is appropriate based on the use of SVI feret diameter and a typical particle aspect ratio of 0.60 to 0.70 [Korolev and Isaac, 2003]. A priori covariances between ϕ and other state variables are unknown and were set to zero.

4. Observation Vector and Synthetic Cases

The observations to be fitted by the retrieval are the reflectivity, the snowfall rate, and the fall speeds. To avoid giving excess weight to the potentially numerous fall speed observations, representative fall speeds are used for three predetermined size (D_M) ranges: V_0 : 4.0 ± 0.50 mm, V_1 : 2.0 ± 0.25 mm, and V_2 : 1.0 ± 0.25 mm. These ranges were chosen on an ad hoc basis to describe the shape of a typical fall speed curve with enough separation in size to minimize redundant information. The wider bin at the largest size was needed to ensure an adequate number of particle in most of the retrievals.

Given the three fall speeds, two fall speed differences are synthesized for use in the observation vector: $\Delta V_1 = V_0 - V_1$ and $\Delta V_2 = V_0 - V_2$. The resulting observation vector uses V_0 and the two differences, giving

$$\mathbf{y} = [Ze \ P \ V_0 \ \Delta V_1 \ \Delta V_2]^T. \quad (17)$$

Here and in the remaining text, Ze is in decibel units unless noted otherwise.

4.1. Synthetic Cases

The retrieval is evaluated by applying it to synthetic cases derived from the C3VP observations. The cases are based on analyses of VertiX reflectivities, FD12P snowfall rates, SVI size distributions, and 2DVD fall speeds for four snowfall events that occurred on 6 and 7 December 2006, 28 January 2007, and 14 February 2007. The analyses, details of which are given in section A, provide estimates of coincident 5 min averaged observations and their uncertainties for these events. The cases were constructed using five snowfall regimes selected to encompass the extent of conditions observed during C3VP. These regimes were selected as shown in Figure 2 using ranges of radar reflectivity and snowfall rate. The regimes represent conditions ranging from light snow with low reflectivity to heavy snow with corresponding high reflectivity, as well as several intermediate conditions.

Each regime was characterized by values for radar reflectivity, snowfall rate, size distribution parameters, and temperature (Table 2). For a particular regime, the characteristic values for radar reflectivity, snowfall

studies are generally fitted to observations of multiple particles of a particular type. The number of observations and the associated time intervals likely vary from type to type. To avoid making the a priori constraint overly restrictive, one might consider enlarging the variances and covariances to broaden the a priori distribution. For these data, the variances are moderately large compared to the expected values (Table 1) and this was not done. Additionally, the frequencies of particle types in the sample did not appear unreasonable, with aggregates and branched planar particles appearing most frequently (totalling 60% for the mass sample and 76% of the area sample), followed by plates, graupel, and columnar particles.

Lacking direct observations of ϕ , a priori values for ϕ and its variance were estimated based on the particle

Table 2. Characteristics of Synthetic Regimes

Regime	Description	Z_e (dB)	P (mm LWE h ⁻¹)	$\log(N_0)$ (m ⁻³ mm ⁻¹)	λ (mm ⁻¹)	T (K)	u (9m s ⁻¹)
A	Very light snow	5.54	0.13	4.17	2.81	263.	3.1
B	Light snow	16.0	0.405	3.66	1.31	261.	3.2
C	Moderate snow, low dBZe	22.0	1.02	3.42	0.835	263.	2.6
D	Moderate snow, high dBZe	28.9	1.11	2.81	0.517	271.	3.0
E	Heavy snow	24.8	2.70	4.43	1.017	265.	2.1

rate, and temperature were determined as simple means of the observations within the associated subset. For the size distribution parameters, an exponential size distribution was fitted to each SVI size distribution in the subset, giving a range of values for the intercept $N_0(D_{\text{obs}})$ and slope $\lambda(D_{\text{obs}})$. The characteristic values for the size distribution parameters were then determined as the simple means of these fitted values and used to compute a synthetic, discrete SVI size distribution $N(D_{\text{obs},i})$ for the regime. To reduce the potential for measurement errors with the surface in situ observations, data were omitted if coincident wind speed observations exceeded 5 m/s. Higher reflectivities and higher snowfall rates were associated with broader distributions (smaller values of λ) (Table 2). Corrections were made to account for the separation between the radar and surface in situ observations (section A1); however, this separation does increase the potential for the radar measurement to be inconsistent with the surface observations, and uncertainties were adjusted as described.

For each regime, synthetic cases were constructed by applying a predefined set of assumed values for the exponents of the mass- and area-dimension relationships, β and σ , and for ϕ (Table 3). These values were selected to span the expected ranges for these variables, using the a priori values plus or minus approximately 1 standard deviation. Given the values for the discrete exponential size distribution $N(D_{\text{obs},i})$ associated with a particular regime, an assumed value for ϕ was used to construct an equivalent exponential distribution based on the maximum dimension, $D_{M,i}$ [Wood et al., 2013]. Using this $N(D_{M,i})$ and the regime's radar reflectivity along with the assumed value for β , the corresponding value for α was found via (9). Because particle masses are capped to be no larger than the masses of equal-diameter ice spheres, a nonlinear least squares fitting routine was used to determine α . Next, taking the assumed value for σ , the corresponding value for γ was found via (13), again using a nonlinear least squares technique due to the dependence of snowfall rate on fall speed and due to the cap on particle area. Finally, synthetic single-particle fall speed data sets were constructed using MH05, with the abundance of particles of different sizes determined by $N(D_{M,i})$ and appropriate 2DVD sample volumes.

Synthetic cases are labeled by the regime, followed by a sequence of characters indicating the values of β , σ , and ϕ , in that order (e.g., following Table 3, "BP0m" indicates regime B, using the values $\beta = 2.6$, $\sigma = 1.785$, and $\phi = 0.725$). Combination of the five regimes with the assumed values of β , σ , and ϕ provided a total of 225 possible synthetic cases; however, 31 combinations did not result in usable cases. For these failed cases, the causes of failure were either that α could not be made large enough to match the desired radar reflectivity due to the cap on particle mass (6 cases), that γ could not be made large enough to match the desired snowfall rate due to the cap on particle area (21 cases), or that γ could not be made small enough to match the desired snowfall rate (4 cases).

Table 3. Values of State Variables Used to Generate Synthetic States and the Textual Labels Used to Identify Them^a

Variable	Values and Labels
β	"M":1.6, "m":1.9, "0":2.067, "p":2.3, "P":2.6
σ	"m":1.6, "0":1.785, "p":2.0
ϕ	"m":0.725, "0":0.825, "p":0.925

^aLabels of "0" indicate values which are equal to the a priori values used in the snow microphysics retrieval.

5. Forward Model and Uncertainties

The relationships between microphysical properties and observations defined by (9) through (15), with caps on mass and area as described previously, define the forward model for the retrieval. Given some discrete size distribution, radar reflectivity is modeled using a discrete form of (9). Fall speeds are modeled for the discrete size distribution size bins using MH05, and snowfall rates are computed via a discrete

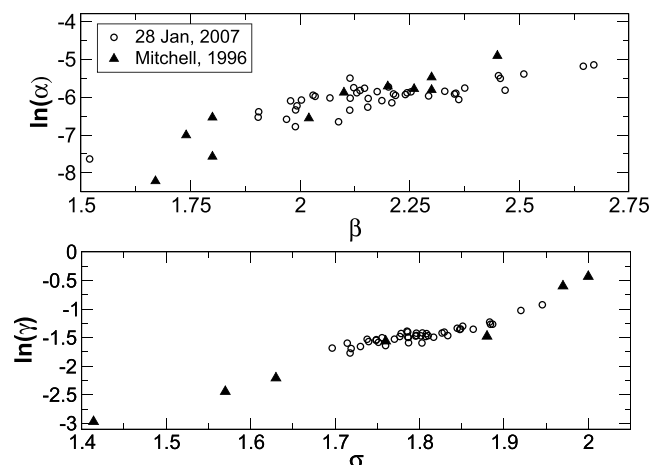


Figure 3. Retrieved values of coefficients and exponents for (top) mass and (bottom) horizontally projected area power functions for the 28 January snowfall event. Also shown for comparison are values from Mitchell [1996] for larger, aggregate-like particles. Values are appropriate for cgs units.

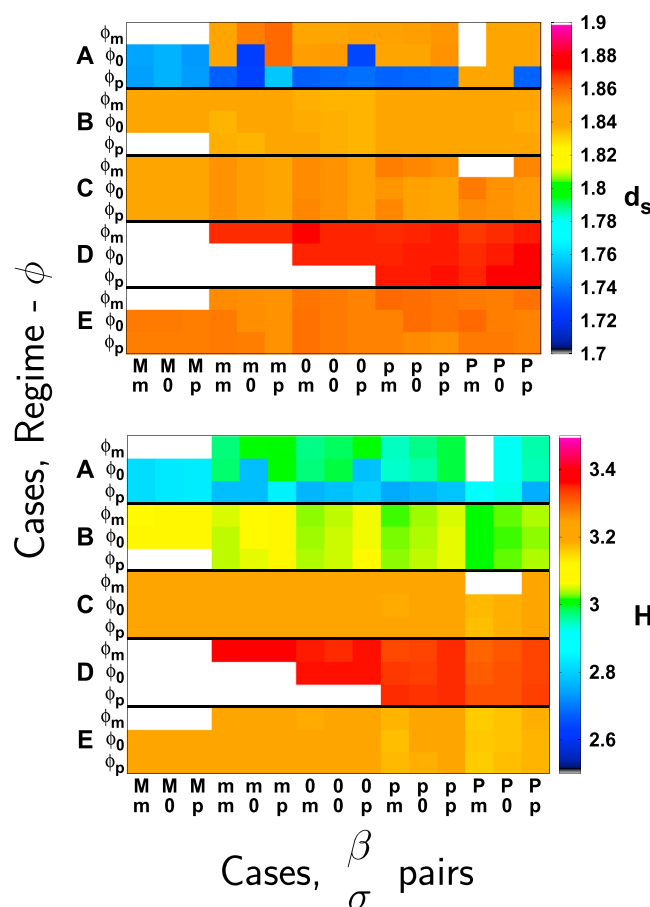


Figure 4. Information content metrics for the synthetic cases. For each panel, the abscissa gives the values of β and σ for the synthetic case, while the ordinate gives the regime and ϕ value, using the labels provided in Table 3. White regions of these panels show synthetic case configurations which did not result in usable cases.

form of (13). Fall speeds are calculated using MH05 for each of the nominal sizes for V_0 , V_1 , and V_2 , then the differences ΔV_1 and ΔV_2 are computed.

The forward model uncertainties are represented by the covariance matrix \mathbf{S}_F . The diagonal elements contain variances for the forward modeled reflectivity, snowfall rate, and fall speed terms. The error covariances in the off-diagonal positions occur between Ze and P because of the common integration over size distribution, and among P and the fall speed terms because of the common dependence on the fall speed forward model. These uncertainties arise because of the discrete treatment of integrals over size distribution (affecting Ze and P), the use of approximate scattering properties (affecting Ze), the approximate treatment of fall speed physics in the MH05 fall speed forward model (affecting P , V_0 , ΔV_1 , and ΔV_2), and uncertainties in other forward model influence parameters including observed size distributions.

Uncertainties due to each of these sources were evaluated with support from SVI and 2DVD observations from C3VP snow events. Further details are provided in section B, where the subsections describe the independent sources of uncertainty. Covariance matrices due to each source were calculated then summed to give \mathbf{S}_F .

6. Retrieval Performance

6.1. Application to C3VP Observations of 28 January 2007

To illustrate the function of the retrieval, results are shown for the lake effect snow event illustrated earlier in Figure 1. This event initially produced light snowfall rates, but rates increased rapidly as a heavy snow band lingered over Canada's Centre for Atmospheric Research Experiments (CARE). Large snowflakes, near 10 mm in diameter, were observed during the periods of heavy snow (R. T. Austin et al., unpublished manuscript, 2007). The retrieved state variables are similar to those reported by Mitchell [1996] for larger, aggregate-like particles (Figure 3). Retrieved values for ϕ were

Table 4. Statistics of Fractional Errors in Percent and Information Content Metrics From the Synthetic Cases^a

Variable or Metric	A Priori		Retrieval		Retrieval HA ^b	
α	−7.1	(37.0)	−5.4	(23.9)	−1.6	(22.8)
β	−0.85	(15.7)	1.0	(10.9)	0.72	(8.0)
γ	−4.5	(49.9)	−4.7	(37.5)	−4.1	(28.6)
σ	0.10	(9.1)	0.87	(8.9)	1.5	(9.4)
ϕ	0.97	(9.9)	0.67	(9.7)	0.3	(9.9)
H	-		3.12	(0.16)	4.57	(0.26)
d_s	-		1.84	(0.034)	2.31	(0.032)

^aMean, followed by standard deviation in parentheses.

^bHigher-accuracy retrieval.

somewhat smaller than the a priori estimate of 0.825, ranging from 0.825 to about 0.75 for this case. Complete results covering additional snow events and the retrieved PDFs for the state variables will be presented in a subsequent paper.

6.2. Synthetic Test Results

The retrieval converged for all of the synthetic test cases and produced chi-square parameters that were acceptable. The degrees of freedom for signal shows that only about two independent and significant quantities are directly constrained by the observations, and, with $H \approx 3$ for most of the synthetic cases, about eight distinct states might be discernible within the a priori state space (Figure 4 and Table 4). H varies principally with the regime, with regimes consisting of lighter snow and lower reflectivity having somewhat smaller values of H than those consisting of heavier snow and higher reflectivity. This behavior may be because the heavier snow regimes have broader distributions which might help constrain the exponents of the mass- and area-dimension relations. The averaged values of H for each regime show a marked dependence on the size distribution slope (Figure 5). In contrast, d_s varies only weakly over the set of synthetic cases.

In addition to the information content metrics introduced in section 2, the retrieval may also be evaluated by considering the errors in the retrieved state variables. The fractional error of a retrieved state variable \hat{x} is given by

$$\Delta(\hat{x}) = \frac{(\hat{x} - x_t)}{|x_t|} 100\% \quad (18)$$

for variables in linear units and

$$\Delta(\hat{x}) = (\exp(\hat{x} - x_t) - 1) 100\% \quad (19)$$

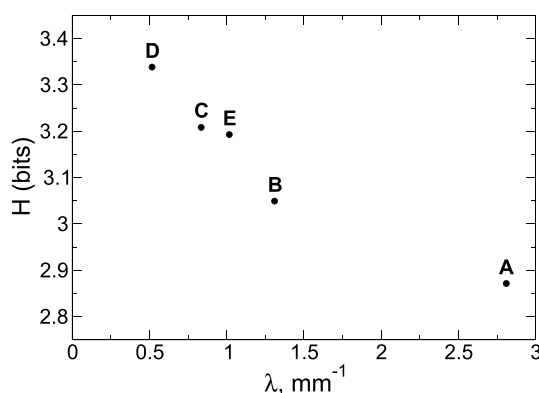


Figure 5. Regime-averaged Shannon information content H versus slope λ of the regime size distribution for the synthetic cases. Each point is labeled with the name of the synthetic regime per Table 2.

for variables in logarithmic units, where x_t is the true value. The errors between the a priori state and the true states for these synthetic cases give the errors that would result if the retrieval did nothing. These errors form the baseline against which the retrieval performance can be evaluated. To compute these errors for the a priori state, the values of \hat{x} in (18) are taken to be the a priori values shown in Table 1.

For the baseline a priori errors, the regular patterns exhibited by the fractional errors for β , σ , and ϕ (Figures 6a, 7a, and 8a) are artifacts of the method used to construct the synthetic cases: the true values for these variables were fixed as shown in Table 3. For α and γ , the true values vary depending on the properties of the

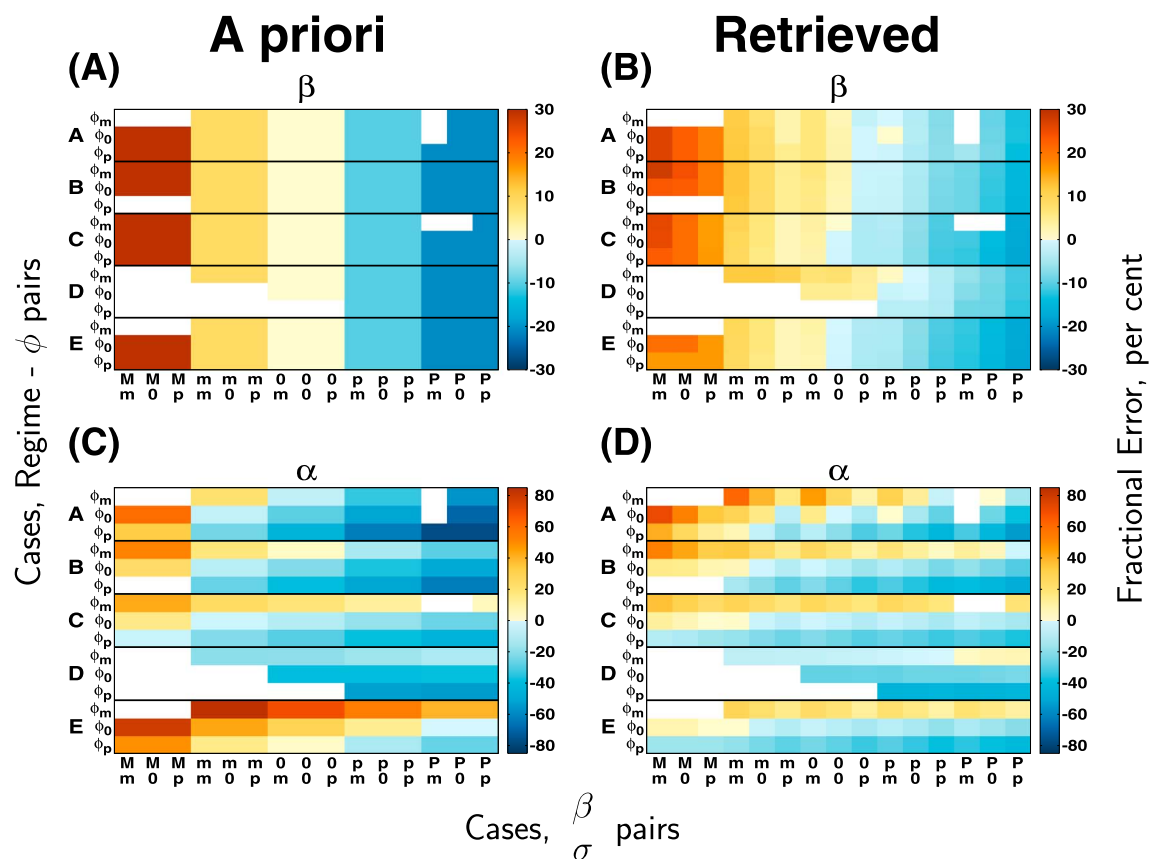


Figure 6. Fractional errors between the true and the (a, c) a priori or (b, d) retrieved mass state variables for synthetic cases. The axes of each panel are as described for Figure 4. White regions show synthetic case configurations which did not results in usable cases.

regime and the values of the other state variables, causing the errors versus the a priori values to vary as well. For α (Figure 6a), a priori errors for each regime vary primarily with β . Errors are predominantly negative when β is larger than its a priori value and positive when β is smaller than its a priori value. This pattern results from the correlation between $\ln(\alpha)$ and β induced by the radar reflectivity forward model and the reflectivity observation.

The largest a priori fractional errors are associated with γ , with errors exceeding +100% in some cases and approaching -70% in others (Figure 7c). The large-magnitude negative errors occur with synthetic cases for which the true value of γ is moderately large (0.5–0.7) compared to the a priori value of 0.211. Many of these cases are for regime D, which combines high reflectivity with moderate snowfall rate. Presumably, γ has been made large for these cases in order to increase the particle area, reducing fall speeds to match the moderate snowfall rate. These cases may not be represented well by the assumptions used in the forward models. In particular, an examination of the subset of observations used to define regime D shows that temperatures for 10 of the 14 members of the subset were in the range of 272 K to 273 K, while the other four were in the range 264 K to 269 K. Those 10 members were observed between 1230 and 1500 UTC on 6 December 2006. Observers on the ground reported wet, sticky snowflakes during this period (R. T. Austin et al., unpublished manuscript, 2007), while the forward model for radar backscattering is appropriate only for dry snow.

Retrieval performance is summarized by the means and standard deviations of the fractional errors for the a priori and retrieved states versus the synthetic true states (Table 4). Since the synthetic true states are distributed in a regular fashion about the a priori state, we expect the means of these errors (i.e., the biases) to be near zero for both the a priori and the retrieval results, and they are. The remaining discussion of these results focuses on changes in the standard deviations.

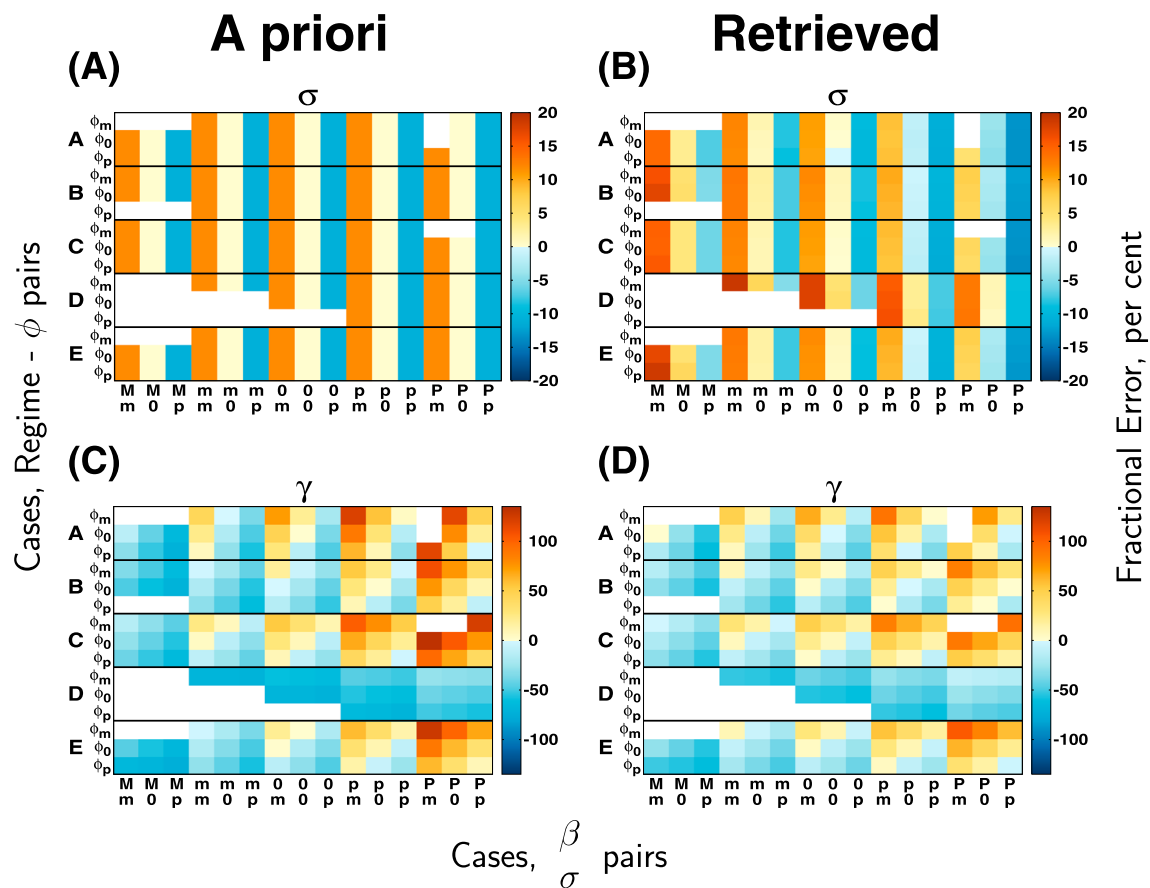


Figure 7. Fractional errors between the true and the (a, c) a priori or (b, d) retrieved area state variables for synthetic cases. The axes of each panel are as described for Figure 4. White regions show synthetic case configurations which did not results in usable cases.

For the mass state variables, the retrieval generally improves upon the a priori. Evaluated over all the synthetic cases, the standard deviation of the fractional errors for β decreases from 15.7% to 10.9% (Table 4). The retrieval reduces errors in β for most of the synthetic cases (Figures 6b versus 6a), particularly those for which the a priori error was large. The left side of Figure 6a shows strong positive errors, while these same regions in Figure 6b show smaller positive errors. Similar comparisons can be made for the right side of Figure 6a, where the a priori errors are strongly negative. Performance is similar for all regimes.

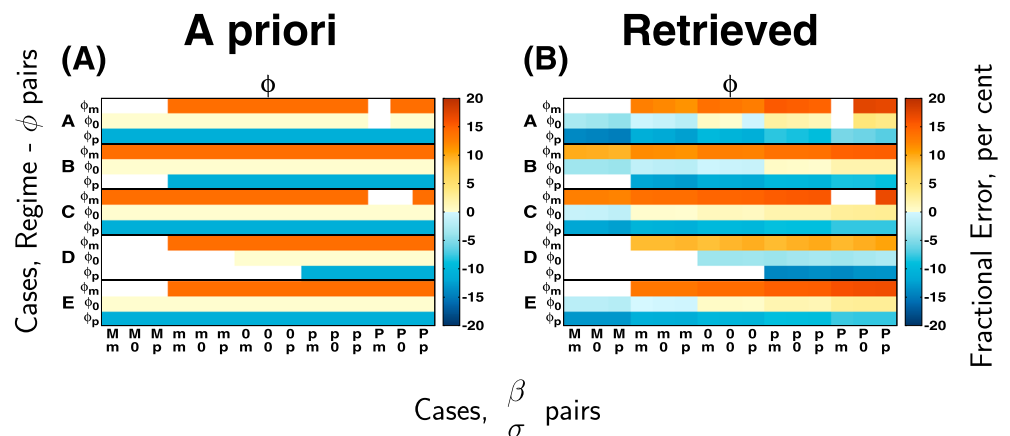


Figure 8. Fractional errors between the true and the (a) a priori or (b) retrieved ϕ for synthetic cases. The axes of each panel are as described for Figure 4. White regions show synthetic case configurations which did not results in usable cases.

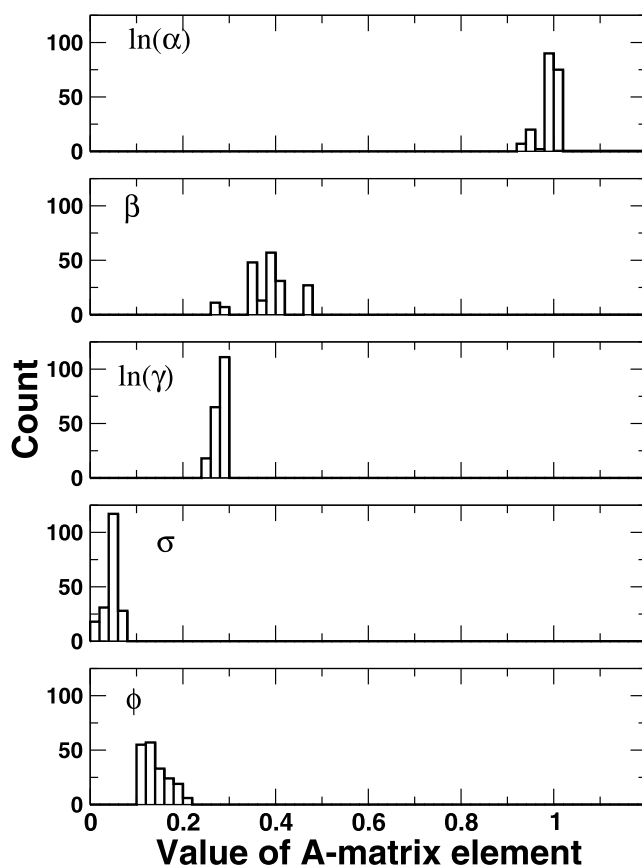


Figure 9. Diagonals of **A** for synthetic cases.

from the synthetic snowfall rates and fall speed observations are not sufficient to steer the retrieval nearer the true state.

The retrieval performance for the remaining state variables is mixed. Similar to the results for α , the standard deviation of the fractional errors for γ decreases substantially, from 49.9% to 37.5%, and the retrieval reduces the error for most of the synthetic cases (Figures 7c and 7d). The performance for σ and ϕ is poorer. The retrieval leaves the standard deviations of their fractional errors almost unchanged. For σ , the results are mixed for different synthetic cases, with some having increased and some having decreased errors (Figures 7a and 7b). For ϕ , the changes in fractional errors between the a priori and retrieved states (Figures 8a and 8b) are minor with the exception of regime D.

These results suggest that $\ln(\alpha)$, β , and $\ln(\gamma)$ are modestly constrained by the retrieval, while the measurements provide little information regarding σ and ϕ . To demonstrate this, the diagonal elements of **A** are examined in Figure 9. Values for $\ln(\alpha)$ are near 1.0, indicating that its retrieved state is determined largely by the observations. In contrast, values for σ are less than 0.1, indicating its retrieved state is determined largely by the a priori. The values of the **A** diagonal elements for the remaining state variables fall between 0.1 and 0.5, indicating that the retrieved state for these variables is determined jointly by the observations and the a priori estimate of the state.

6.3. Uncertainties and Observing System Design

The information content metrics provided by the microphysics retrieval provide a concise way to quantify the influence of changes in the observing system on the retrieval performance. For the observations themselves, significant uncertainties arise because of ground clutter in the VertiX radar profiles, the lack of replicate observations of snowfall rate, and the relatively small sample volume of the SVI. Additionally, uncertainties in the fall speed forward model were substantial, estimated at 30% of the observed fall speeds. Using the synthetic test cases, an experiment was performed in which a series of improvements was applied

For α , the standard deviation of the fractional errors decreases from 37.0% to 23.9%. Again, the retrieval reduces errors for most of the synthetic cases (Figures 6b versus 6c). The exceptions are for regime A (light snow) accompanied by small values of ϕ and/or small values of β and regime E (heavy snow) accompanied by large values of ϕ and β . These cases depart substantially from the a priori state, and the ability of the retrieval to find solutions far from the a priori is limited. As an example, case Eppp has a true state with $\alpha = 0.00279$ and $\beta = 2.6$, while the a priori has $\alpha = 0.002078$ and $\beta = 2.067$. Applying the true state to the size distribution defined for regime E (Table 2) gives a reflectivity of 24.8 dBZe, while applying the a priori state gives 27.2 dBZe. Therefore, the retrieval must reduce the reflectivity by changing α and β from the a priori values; however, instead of substantially increasing β , the retrieval makes a modest increase to $\beta = 2.14$ and reduces α to 0.00167. The retrieved state gives a reflectivity of 24.5 dBZe, near the desired value. In this case, the remaining constraints

Table 5. Changes in Information Content Metrics Due To Improvements in Observational and Forward Model Uncertainties

	Initial	Improvement			
		Ze	P	$N(D)$	Fall Speed
H	3.12	3.67	3.67	3.68	4.57
d_s	1.84	1.90	1.91	1.91	2.31

that the radar observation is representative of the surface in situ observations and allows the proximity uncertainties described in section A1 to be omitted. Next, the uncertainties for the observed FD12P snowfall rates can be reduced to half their values, simulating the improvements that would result from having four replicate snowfall rate observations. Third, we can assume more accurate size distributions, equivalent to increasing the SVI sample volume by a factor of 6. This could be achieved by deploying additional instruments, by enlarging the field of view or depth of field of the SVI camera, by increasing the sample times, or by a combination of these changes. Finally, a more accurate fall speed model may be simulated, with uncertainties reduced from 30% to 10% of observed fall speeds.

Results of these tests are shown in Table 5. Original values of H and d_s are shown, along with the new values resulting from incrementally applying the improvements. The improvements to the observations themselves led to negligible increases in d_s but do introduce modest improvements in H . This result is consistent with the interpretation of degrees of freedom for signal and information content. Reducing uncertainties in existing measurements does not introduce new independent information but does allow the retrieval to better resolve the retrieved state. Improvements to the fall speed forward model, however, produced substantial improvements in H and more significant improvements in d_s . Not only is the retrieved state better resolved, but the retrieval is utilizing more of the information available in the observations.

Changes in the retrieval fractional uncertainties are consistent with the improvements. When all improvements are applied, including the key reduction in fall speed forward model uncertainties, the standard deviation of the fractional uncertainties in γ is reduced to 28.6% (Table 4) although changes in other standard deviations are negligible. Since the radar reflectivity partially constrains the mass parameters, the improved fall speeds then provide improved constraints on A_p and its parameters per (15).

7. Conclusions

The snow microphysics retrieval represents a novel approach to integrating independent observations of Rayleigh-regime radar reflectivity, snowfall rate, particle fall speeds, and size distributions to extract snow microphysical properties. Traditional processes for determining these properties can be onerous (e.g., measuring diameters of melted drops to determine the mass of individual particles) or make less complete use of the observations to look at limited aspects of the microphysical properties (e.g., 2DVD disdrometer estimates of snow particle volume combined with precipitation accumulation to estimate snow particle bulk density). The snow microphysics retrieval produces estimates of size-dependent particle mass and area that give a consistent representation of Rayleigh scattering properties, fall speeds, and snowfall rate for a population of particles. Additionally, these estimates are constructed as PDFs. These PDFs provide information about the variability and uncertainties of these properties that are critical elements in satellite snowfall retrievals [e.g., Liu, 2008; Kulie *et al.*, 2010; Skofronick-Jackson *et al.*, 2004].

The retrieval was tasked with determining five pieces of information ($\ln(\alpha)$ and β for mass, $\ln(\gamma)$ and σ for area, and ϕ) from five observations (Ze , P , V_0 , ΔV_1 , and ΔV_2). The information content metrics from synthetic tests showed that, given the a priori information, only about two independent and significant pieces of information were provided by the measurements. The measurements contributed principally to the determination of $\ln(\alpha)$, with less significant contributions to the determination of β and $\ln(\gamma)$. Relatively little information was provided for σ and ϕ . Nevertheless, the inclusion of ϕ was found to be essential for correct performance of the retrieval. For an observing system with these capabilities, the results highlight the importance of traditional particle measurements. Such measurements could better constrain the a priori distributions of these variables or, integrated into field campaigns like C3VP, could serve to independently evaluate retrieval results.

to these uncertainties and the information content metrics reevaluated to quantify the components of the observing system that may offer the greatest potential for improving the retrieval performance.

Suppose, for example, that reflectivity observations could be made with reduced ground clutter contamination, allowing the observed reflectivity to be nearer the surface observations of snowfall rate, size distribution, and fall speeds. This insures

Information content metrics were used to characterize the benefits that might be achieved by improvements to various aspects of the observations and the retrieval. While modest improvements in retrieval performance were obtained by reducing ground clutter, improving snowfall rate accuracies, and increasing SVI sample volume, the most significant improvements were achieved when the fall speed forward model uncertainties were reduced. Targeted improvements to fall speed modeling, such as through the use of particle imagery to adjust for particle geometry effects [e.g., *Heymsfield and Westbrook*, 2010], offer significant potential for improving future observing systems. The sensitivity of the information content metrics to the uncertainties in the fall speed forward model suggests that expanding the number of fall speed observations in the observation vector might also improve retrieval performance.

Appendix A: Analyses of C3VP Observations

C3VP [Hudak *et al.*, 2006a], held in south-central Ontario during Northern Hemisphere winter 2006/2007, established an enhanced surface measurement site at the Meteorological Service of Canada's Centre for Atmospheric Research Experiments (CARE) at Egbert, Ontario, approximately 80 km north of Toronto. Nearly coincident observations of near-Rayleigh radar reflectivity, snowfall rate, size-resolved fall speeds, and size distributions were available for four snow events which occurred on 6 and 7 December 2006, 28 January 2007, and 14 February 2007. Fall speed observations were available for three additional events which occurred on 17, 20, and 22 January 2007. The events included both lake effect and synoptic front-driven snowfall. Observations from these events were used to characterize synthetic snowfall regimes and to estimate observational uncertainties for testing the retrieval. Reflectivity, snowfall rate, and fall speeds form the retrieval's observation vector and are discussed here. Size distributions are forward model parameters and are discussed in section B.

A1. Radar Reflectivity

The McGill University Vertically Pointing X-band Doppler Radar (VertiX) [Fabry and Zawadzki, 1995] provided vertical profiles of reflectivity at 9.35 GHz, a frequency at which scattering by snow particles is expected to be near-Rayleigh, with 37.5 m vertical resolution and 10 s temporal resolution. VertiX observations were calibrated via comparisons against coincident observations of snowfall over CARE from the MSC King City C-band radar (WKR) [Hudak *et al.*, 2006b]. While a hardware failure degraded VertiX performance early in C3VP, the calibrated reflectivities after repair showed a standard error of 0.15 dB relative to WKR [Wood, 2011]. The calibrated VertiX reflectivities were averaged in linear units to 5 min temporal resolution to match the SVI observations then converted to dBZe.

Due to ground clutter, the first 12 range bins were unusable during most snowfall conditions, causing a vertical separation of 488 m between the reflectivity observations and the surface. This separation induces a time delay between the appearance of a precipitation feature aloft and its appearance at the surface and allows microphysical processes to change the snow properties and the reflectivity as the feature descends from bin 13 to the surface.

Reflectivities at the surface were extrapolated from the reflectivities observed in bin 13 using an adjustment as described by Wood [2011]. The adjustment involves correcting for time delays then evaluating the vertical reflectivity gradient in the delay-corrected radar profiles. Uncertainties were estimated by applying a similar adjustment between bins 25 and 13, then comparing the estimated and observed reflectivities for bin 13. The standard deviation of the reflectivity errors ranged from 2.0 to 3.6 dB, and 2.5 dB was taken as a typical uncertainty.

A2. Snowfall Rate

The principal observations of snowfall amounts at CARE were made by a manual Tretyakov gauge installed within a vertical octagonal double fence, known as a double fence intercomparison reference (DFIR) [Goodison *et al.*, 1998]. Observations were recorded each day at 1300 and 2100 UTC. The DFIR was located approximately 200 m from the main instrument cluster at CARE, where precipitation rate measurements at 1 min resolution were made by a Vaisala FD12P [Vaisala, 2002]. For each snowfall event used, the FD12P rates were scaled to match the DFIR accumulations calculated from 2100 UTC the day before the event to 1300 UTC the day after the event. The FD12P consistently underestimated accumulations relative to the DFIR, with ratios (DFIR/FD12P) ranging from 1.15 to 1.98. The 1 min FD12P snowfall rates were averaged to 5 min resolution.

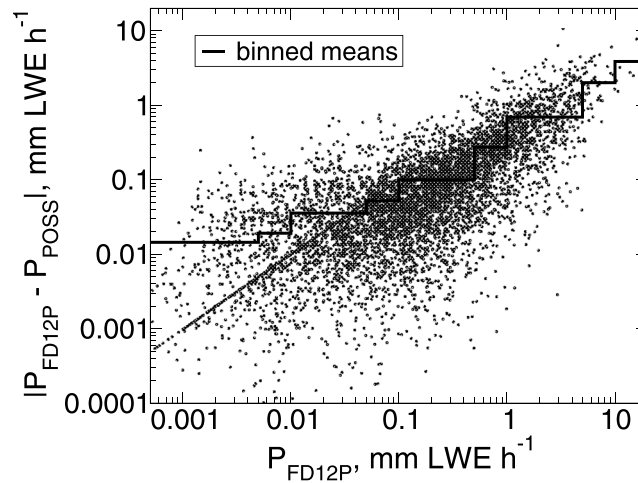


Figure A1. Absolute differences in precipitation rates between the FD12P and POSS instruments and binned mean differences used to estimate uncertainties in precipitation rates (heavy line). Precipitation rates are 5 min averages.

σ to MH05. The uncertainties in these synthetic fall speeds are estimated using actual observations from Colorado State University's 2-D Video Disdrometer [Thurai and Brangi, 2005]. The 2DVD captures particle images from two vertically separated line scan cameras. Fall speeds can be calculated if the two images produced by a particle can be matched. The data used here are from the improved matching algorithm of Huang *et al.* [2010] for the four C3VP snowfall events supplemented with three additional events: 17, 20, and 22 January 2007. For each pair of matched images, the data provide the maximum particle width from each of the two images along with the particle's fall speed. The particle size $D_{2DVD,w}$ is taken as the larger of these two maximum widths. In actual use, $D_{2DVD,w}$ is converted to D_M using a factor similar to ϕ for the SVI. Since the factor varies weakly with particle shape for the 2DVD [Wood *et al.*, 2013], a constant value is used, with $D_M = D_{2DVD,w}/0.95$.

The 2DVD data for the seven events were composed into 5 min samples. For each sample, the particles within each of the three designated size ranges (section 4) were filtered [Brandes *et al.*, 2008], then the sample mean fall speed and its variance were calculated for each size range. The fall speed uncertainty for each size range was taken to be the square root of the variance of the sample mean.

Assuming that the observational errors in the mean fall speeds for different size ranges are uncorrelated, the required variances and covariances for the fall speed terms in the observation vector can be found as

$$\begin{aligned} s_y^2(\Delta V_1) &= s_y^2(V_0) + s_y^2(V_1) \\ s_y^2(\Delta V_2) &= s_y^2(V_0) + s_y^2(V_2) \\ s_y(V_0, \Delta V_1) &= s_y^2(V_0) \\ s_y(V_0, \Delta V_2) &= s_y^2(V_0) \\ s_y(\Delta V_1, \Delta V_2) &= s_y^2(V_0) \end{aligned} \quad (A1)$$

where $s^2(\cdot)$ and $s(\cdot, \cdot)$ represent variances and covariances, respectively.

Averaging over all 5 min samples gave values of $s_y^2(V_0) = 0.0429^2$, $s_y^2(\Delta V_1) = 0.0533^2$, and $s_y^2(\Delta V_2) = 0.0522^2$, with fall speed in m s^{-1} .

Appendix B: Forward Model Uncertainties

B1. Discretization and Truncation

Wood *et al.* [2013] used 2DVD observations from C3VP to estimate errors due to discretization and truncation in X-band reflectivity calculated from discrete SVI size distributions. When power functions are used to describe particle mass, the biases and uncertainties are largely dependent on the exponent of the power

Lacking observations from replicate FD12P instruments, uncertainties for the FD12P were evaluated by comparing against snowfall rate estimates from a Precipitation Occurrence Sensor System (POSS) [Sheppard and Joe, 2008], similarly scaled to match DFIR accumulations (Figure A1). For rates less than 0.05 mm h^{-1} , uncertainties were found to be 0.03 mm h^{-1} . For larger rates up to 0.5 mm h^{-1} , uncertainties were estimated to be 50% of the observed rate, while for rates larger than 0.5 mm h^{-1} , uncertainties were found to be 30% of the observed rate.

A3. Size-Resolved Fall Speeds

Size-resolved fall speeds for the synthetic cases are obtained by applying the specified values of α , β , γ , and

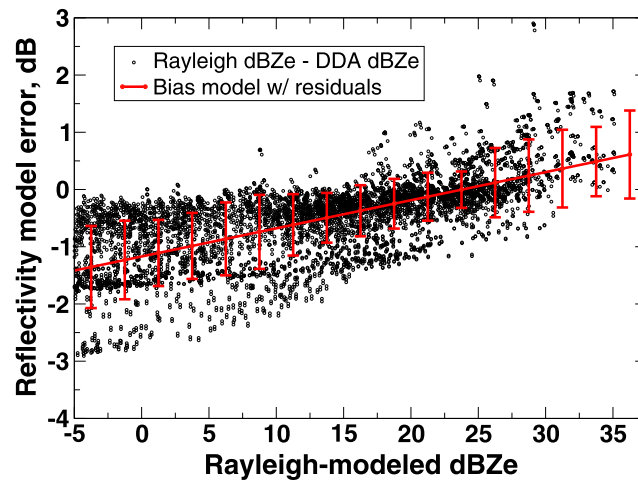


Figure B1. Rayleigh model errors relative to reflectivities calculated using DDA scattering properties for observed SVI size distributions. Points show the difference between Rayleigh modeled reflectivity and DDA-modeled reflectivity for each size distribution observation. The fitted line shows a linear estimate of the bias, while the error bars show the root-mean-square error calculated from the residual differences after bias correction.

function. For 5 min samples and trapezoidal integration using size bin widths $\Delta D_M = 0.25$ mm, a simple linear fit to those results gives

$$\begin{aligned}\overline{\delta_F(Ze)} &= -0.26\beta - 0.38 \\ s_F^2(Ze) &= (0.99\beta - 0.78)^2\end{aligned}\quad (B1)$$

where $\bar{\delta}$ indicates bias.

A similar analysis of fractional errors in snowfall rate provides

$$\begin{aligned}\overline{\delta_F(P)} &= (-0.023\beta + 0.083)P \\ s_F^2(P) &= (0.14P)^2,\end{aligned}\quad (B2)$$

with error covariances between the reflectivity and snowfall rate given by

$$s_F(Ze, P) = 0.35 (s_F(Ze)) (s_F(P)). \quad (B3)$$

B2. Uncertainties Due To Backscattering Properties

To evaluate uncertainties due to snow particle scattering properties, reflectivities calculated using the Rayleigh approximation for ice spheres were compared against reflectivities calculated from scattering properties obtained using the discrete dipole approximation (DDA) model DDSCAT (version 6.1) of *Draine and Flatau* [1994] for a variety of particle shapes as described by *Wood* [2011]. DDA calculations were performed for several distinct pristine habits and also for aggregate-like particles. Pristine habits were constructed using various mass, dimensional and density relations from prior observational studies [*Auer and Veal*, 1970; *Heymsfield*, 1972; *Mitchell*, 1996]. The aggregate-like particle was a spatially branched shape. This shape was used to construct several different examples of aggregates by using mass-dimension relations appropriate for aggregates [*Locatelli and Hobbs*, 1974] and using the “Aggregate hybrid approach” of *Heymsfield et al.* [2002] to determine the horizontally projected area. The DDA scattering properties extend to radiative size parameters $x = 0.99$ (based on particle maximum dimension D_M) or $x = 0.096$ (based on the diameter of an equivolume ice sphere) where

$$x = \frac{\pi D}{\lambda}. \quad (B4)$$

D is a measure of particle size, and λ is wavelength.

An ensemble of test cases was constructed using 978 SVI size distributions observed during C3VP snow events. Reflectivities were calculated using both the Rayleigh sphere approximation and using the DDA scattering properties assuming pristine shapes for small particles and aggregate shapes for large particles [*Wood*, 2011]. The DDA reflectivities are generally larger than the Rayleigh model when reflectivities are small and slightly smaller than the Rayleigh model when reflectivities are large (Figure B1). Averaged over the ensemble of test cases, the bias of the Rayleigh sphere reflectivities relative to the DDA reflectivities ranges from -1.5 dB at -5 dB to $+1.0$ dB at 35 dB. The root-mean-square values of the residual errors after bias correction vary between 0.2 and 0.6 dB over the same range. Consolidating all the ensemble states, a linear bias correction was determined to be

$$\overline{\delta_F(Ze)} = -0.049Z_{\text{Rayl}} - 1.17, \quad (B5)$$

where Z_{Rayl} is the reflectivity in dB modeled using Rayleigh spheres and the corresponding variance was modeled as $s_F^2(Ze) = 0.42$.

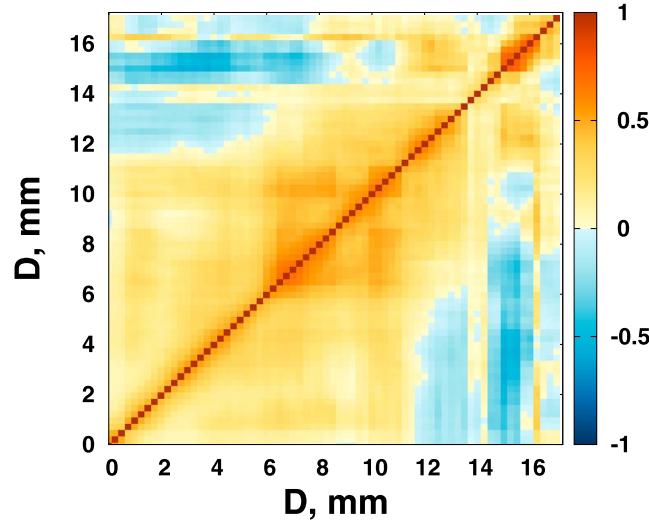


Figure B2. Fall speed forward model error correlations for MH05, after application of a 5 bin \times 5 bin moving window average.

B3. Fall Speeds

Uncertainties due to approximations in the forward model for fall speeds are difficult to assess, as there are no higher-quality fall speed models against which to compare. In their study of previously reported laboratory and in situ measurements of ice particle fall speeds, *Heymsfield and Westbrook* [2010] estimated the uncertainty of fall speeds calculated with their method to be less than 30%, developing their estimate by binning single-particle fall speed errors by area ratio and determining the median fall speed error. *Mitchell and Heymsfield* [2005] did not provide a similar estimate; however, examining the scatter in the Reynolds numbers of observed particles about their model (their Figure 2)

suggests that 30%–50% uncertainty is not unreasonable. Accordingly, an uncertainty of 30% was adopted for modeled fall speeds.

The contribution to \mathbf{S}_F due to the fall speed forward model uncertainties is given by

$$\mathbf{S}_{F,v} = \mathbf{K}_v \mathbf{S}_v \mathbf{K}_v^T, \quad (\text{B6})$$

where \mathbf{K}_v is the Jacobian of the forward model with respect to the fall speeds and \mathbf{S}_v is the fall speed error covariance matrix. The first row of \mathbf{K}_v , $\partial Z_e / \partial \mathbf{v}$, is uniformly zero since Z_e has no dependence on the fall speeds. The second row, $\partial P / \partial \mathbf{v}$, follows the numerical treatment used to integrate (13), and with trapezoidal integration becomes

$$\frac{\partial P}{\partial \mathbf{v}} = \frac{1}{\rho_{\text{liq}}} \left[N(D_{M;0}) m(D_{M;0}) \frac{\Delta D_{M;0}}{2} \right. \\ N(D_{M;1}) m(D_{M;1}) \Delta D_{M;1} \cdots \\ \left. N(D_{M;K}) m(D_{M;K}) \frac{\Delta D_{M;K}}{2} \right], \quad (\text{B7})$$

where K is the number of discrete bins in the size distribution and $\Delta D_{M;i}$ are the widths of the size bins. In the third row, $\partial V_0 / \partial \mathbf{v}$ has a value of one at the size bin at which V_0 is defined (i.e., at $D_M = 4$ mm) and is zero elsewhere. The fourth and fifth rows are obtained similarly as $\partial (V_0 - V_1) / \partial \mathbf{v}$ and $\partial (V_0 - V_2) / \partial \mathbf{v}$.

The estimate of forward model fall speed uncertainties given above requires covariances of the fall speed model errors as a function of particle size, \mathbf{S}_v . Lacking a higher-quality forward model, estimates of \mathbf{S}_v were obtained by performing simple fits of the MH05 fall speed forward model to the observed 2DVD fall speeds, then evaluating correlations between the fitting errors. The fall speeds from 5 min samples from the seven events were binned into the same size distribution bins used by the SVI, then filtered [*Brandes et al.*, 2008] before means and standard errors were calculated. The fall speed forward model was then fitted to the mean fall speeds using a nonlinear least squares technique, and fitting errors were found for each size bin. Paired errors (error for size bin i paired with error for size bin j) were collected for each sample over all samples, then correlations between errors were calculated, forming a fall speed error correlation matrix ρ_v . A 5 bin \times 5 bin moving window average was applied to smooth the variations (Figure B2). From the error correlation matrix, the values of the elements of the error covariance matrix \mathbf{S}_v are

$$s_v^2(v_i, v_j) = \rho_v[i, j] f^2 v_i v_j, \quad (\text{B8})$$

where f is the fractional error for the fall speeds, taken to be 30% as noted above, with v_i and v_j the fall speeds for size bin i and bin j .

Table B1. Influence Parameter Dependencies of the Forward Model Components

Component	Parameters
Ze	$D_i, N(D_i), \ K_i\ ^2$
P	$D_i, N(D_i), T, p, \delta_0, C_0, a_0, b_0$
V_0	$T, p, \delta_0, C_0, a_0, b_0$
ΔV_1	$T, p, \delta_0, C_0, a_0, b_0$
ΔV_2	$T, p, \delta_0, C_0, a_0, b_0$

B4. Uncertainties Due to Influence Parameters

Influence parameters that must be assumed in the forward model include not only the density of ice and the dielectric properties of ice and water, which are reasonably well determined, but also the discrete values of the size distribution $N(D_{M,i})$, the associated sizes D_i , and environmental properties like temperature and pressure. \mathbf{S}_B is found as

$$\mathbf{S}_B = \mathbf{K}_b \mathbf{S}_b \mathbf{K}_b^T, \quad (\text{B9})$$

where \mathbf{K}_b is the Jacobian of the forward model with respect to the influence parameters and \mathbf{S}_b is the influence parameter uncertainty covariance matrix. Since \mathbf{K}_b varies with the estimated state variables, \mathbf{S}_B is evaluated as the retrieval iterates.

Parameter dependencies shared by the forward model components will result in covariances between errors in the forward modeled observation vector variables. Table B1 summarizes the parameter dependencies of the forward model components. Dependencies on T and p , atmospheric temperature and pressure, arise through the dependence of fall speeds on atmospheric density and viscosity. Although $\|K_i\|^2$ exhibits a dependence on temperature which would cause Ze to also be dependent on temperature, this dependence is weak over the expected atmospheric temperature range and is ignored.

Parameter dependencies shared by the forward model components will result in covariances between errors in the forward modeled observation vector variables. Table B1 summarizes the parameter dependencies of the forward model components. Dependencies on T and p , atmospheric temperature and pressure, arise through the dependence of fall speeds on atmospheric density and viscosity. Although $\|K_i\|^2$ exhibits a dependence on temperature which would cause Ze to also be dependent on temperature, this dependence is weak over the expected atmospheric temperature range and is ignored.

B4.1. Size Distribution Uncertainties

The Snow Video Imager (SVI) [Newman *et al.*, 2009] uses a video camera to capture 2-D images of particles that fall within the 3-D volume defined by the camera's 2-D field of view and the depth of field. For C3VP, the SVI camera was mounted pointing horizontally, giving elevation views of the snow particles. The SVI size distributions were reported in discrete size bins of width 0.25 mm using the feret diameter, $D_{SVI,f}$, for sizes ranging from 0 to 26 mm at 1 min resolution. To improve the sample volume and reduce uncertainties while maintaining reasonable time resolution, the SVI observations were composited into distinct 5 min samples.

Observational errors in the size distributions arise from a number of sources related to both the analysis of the particle images and to the probabilistic nature of the observations. A method to evaluate these analytic and sampling uncertainties was described by Wood *et al.* [2013] and is the method used in this work. Briefly, analytic uncertainty sources include errors in counting the particles in an image, uncertainties in measured particle size, and uncertainties in the sample volume calculated for each particle. These uncertainties are propagated into uncertainties in the SVI size bins and size distribution values. Sampling uncertainties arise due to statistical fluctuations in the number of particles counted by the instrument. The particle count for a particular size bin is treated as a Poisson random deviate, and the particle sizes are treated as random deviates distributed per a PDF defined by the observed size distribution. Note that while the particle dimension $D_{SVI,f}$ observed by the SVI will, for almost all typical particles, underestimate the true maximum dimension D_M of the particle [Wood *et al.*, 2013], the adjustments to the size distribution to convert $N(D_{SVI,f})$ to $N(D_M)$, and uncertainties in those adjustments are handled separately in the retrieval process via the state variable ϕ .

B4.2. Variances for Other Parameters

The remaining influence parameters for which variances are required are $\|K_i\|^2$, T , p , δ_0 , C_0 , a_0 , and b_0 . The value of $\|K_i\|^2$ used in this work was taken to be 0.177, a value appropriate for 9.35 GHz at 250 K from the compilation of Warren [1984]. The contributions of uncertainties in $\|K_i\|^2$ to uncertainties in the forward modeled reflectivity were neglected as they are likely small compared to uncertainties due to the forward model formulation and to observational uncertainties.

All other parameters affect the calculation of fall speeds. T and p are used to calculate air viscosity, δ_0 and C_0 describe hydrodynamic properties of particles, and a_0 and b_0 are empirical constants used to improve the agreement between the MH05 model and observed fall speeds for aggregate particles [Mitchell and Heymsfield, 2005]. The uncertainties in fall speeds due to uncertainties in a_0 and b_0 were assumed to be subsumed in the uncertainty estimates for the fall speed forward models, so uncertainties in a_0 and b_0 were ignored. Uncertainties in δ_0 and C_0 were obtained by comparing the values found by Heymsfield and Westbrook [2010] against the values used by Mitchell and Heymsfield [2005]. The respective values of δ_0 were 8.0 and 5.83, and those for C_0 were 0.35 and 0.6. The differences (2.17 and 0.25) were used as the

Acknowledgments

Parts of this research by N.B.W. and T.S.L. were performed at the University of Wisconsin–Madison and at Colorado State University for the Jet Propulsion Laboratory, California Institute of Technology, sponsored by the National Aeronautics and Space Administration. A.J.H. acknowledges support from the JPL CloudSat Office and NASA Global Precipitation Measurement program contract NN-X13AH73G. Thanks to G.-J. Huang of Colorado State University (2DVD data), F. Fabry of McGill University (VertiX data), and L. Bliven of NASA Goddard Space Flight Center (SVI data) for making their C3VP data sets available and sharing their expertise. Other data used in the analyses, including the relevant FD12P and DFIR observations, are available from the authors. Thanks to two anonymous reviewers and S. Nesbitt of University of Illinois Urbana–Champaign for their thoughtful comments and suggestions.

estimated uncertainties and were assumed to be uncorrelated. Reasonable uncertainties for T and p are likely to have minimal effects on air viscosity, and nominal uncertainties were taken to be 0.5°C and 1 kPa .

References

- Atlas, D., M. Kerker, and W. Hitschfeld (1953), Scattering and attenuation by non-spherical atmospheric particles, *J. Atmos. Terr. Phys.*, **3**, 108–119.
- Auer, A. H., Jr., and D. L. Veal (1970), The dimensions of ice crystal in natural clouds, *J. Atmos. Sci.*, **27**, 919–926.
- Bohm, H. P. (1989), A general equation for the terminal fall speed of solid hydrometeors, *J. Atmos. Sci.*, **46**, 2419–2427.
- Brandes, E. A., K. Ikeda, G. Zhang, M. Schoenhuber, and R. M. Rasmussen (2007), A statistical and physical description of hydrometeor distributions in Colorado snowstorms using a video disdrometer, *J. Appl. Meteorol. Clim.*, **46**, 634–650, doi:10.1175/JAM2489.1.
- Brandes, E. A., K. Ikeda, and G. Thompson (2008), Aggregate terminal velocity/temperature relations, *J. Appl. Meteorol. Clim.*, **47**, 2729–2736, doi:10.1175/2008JAMC1869.1.
- Davis, C. I. (1974), The ice nucleating characteristics of various Agl aerosols, PhD dissertation, Univ. of Wyoming, Laramie, Wyoming, USA, available from ProQuest Dissertations and Theses. (UMI No. 7423689).
- Draine, B. T., and P. J. Flatau (1994), Discrete-dipole approximation for scattering calculations, *J. Opt. Soc. Am. A*, **11**, 1491–1499.
- Fabry, F., and I. Zawadzki (1995), Long-term radar observations of the melting layer of precipitation and their interpretation, *J. Atmos. Sci.*, **52**, 838–851.
- Goodison, B. E., P. Y. T. Louie, and D. Yang (1998), WMO solid precipitation measurement intercomparison: Final report, World Meteorological Organization Instruments and Observing Methods Report No. 67, WMO/TD - No. 872. 88 pp. plus 212 pp. Annexes.
- Heymsfield, A. J. (1972), Ice crystal terminal velocities, *J. Atmos. Sci.*, **29**, 1348–1357.
- Heymsfield, A. J., and L. M. Miloshevich (2003), Parameterizations for the cross-sectional area and extinction of cirrus and stratiform ice cloud particles, *J. Atmos. Sci.*, **60**, 936–956.
- Heymsfield, A. J., and C. D. Westbrook (2010), Advancements in the estimation of ice particle fall speeds using laboratory and field measurements, *J. Atmos. Sci.*, **67**, 2469–2482, doi:10.1175/2010JAS3379.1.
- Heymsfield, A. J., S. Lewis, A. Bansemmer, J. Jaquinta, L. M. Miloshevich, M. Kajikawa, C. Twohy, and M. R. Poellet (2002), A general approach for deriving the properties of cirrus and stratiform ice cloud particles, *J. Atmos. Sci.*, **59**, 3–29.
- Huang, G.-J., V. N. Bringi, R. Cifelli, D. Hudak, and W. A. Petersen (2010), A methodology to derive radar reflectivity-liquid equivalent snow rate relations using C-band radar and a 2D video disdrometer, *J. Atmos. Oceanic Technol.*, **27**, 637–651.
- Hudak, D., H. Barker, P. Rodriguez, and D. Donovan (2006a), The Canadian CloudSat validation project, *Proceedings of the Fourth European Conference on Radar in Hydrology and Meteorology*, Barcelona, Spain, 609–612. [Available online at <http://www.erad2006.org>.]
- Hudak, D., P. Rodriguez, G. Lee, A. Ryzhkov, F. Fabry, and N. Donaldson (2006b), Winter precipitation studies with a dual polarized C-band radar, *Proceedings of the Fourth European Conference on Radar in Hydrology and Meteorology*, Barcelona, Spain, 9–12. [Available online at <http://www.erad2006.org>.]
- Hudak, D., W. Petersen, G. Skofronick-Jackson, M. Wolde, M. Schwaller, P. Joe, C. Derksen, K. Strawbridge, P. Kollias, and R. Stewart (2012), GPM Cold Season Precipitation Experiment (GCPEX), *Proceedings of Meteorological Satellite Conference*, Sopot, Poland, EUMETSAT, P61_S4_08. [Available online at http://www.eumetsat.int/website/home/News/ConferencesandEvents/PreviousEvents/DAT_2035484.html.]
- Kajikawa, M. (1972), Measurement of falling velocity of individual snow crystals, *J. Meteorol. Soc. Jpn.*, **50**, 577–584.
- Kajikawa, M. (1975), Measurements of falling velocity of individual graupel particles, *J. Meteorol. Soc. Jpn.*, **53**, 476–481.
- Kajikawa, M. (1982), Observation of the falling motion of early snow flakes. Part I: Relationship between the free-fall pattern and the number and shape of component snow crystals, *J. Meteorol. Soc. Jpn.*, **60**, 797–803.
- Korolev, A., and G. Isaac (2003), Roundness and aspect ratio of particles in ice clouds, *J. Atmos. Sci.*, **60**, 1795–1808.
- Kulie, M. S., R. Bennartz, T. J. Greenwald, Y. Chen, and F. Weng (2010), Uncertainties in microwave properties of frozen precipitation: Implications for remote sensing and data assimilation, *J. Atmos. Sci.*, **67**, 3471–3847, doi:10.1175/2010JAS3520.1.
- L'Ecuier, T. S., P. Gabriel, K. Leesman, S. J. Cooper, and G. L. Stephens (2006), Objective assessment of the information content of visible and infrared radiance measurements for cloud microphysical property retrievals over the global oceans. Part I: Liquid clouds, *J. Appl. Meteorol. Clim.*, **45**, 20–41.
- Liu, G. (2008), Deriving snow cloud characteristics from CloudSat observations, *J. Geophys. Res.*, **113**, D00A09, doi:10.1029/2007JD009766.
- List, R., and R. S. Schemenauer (1971), Free-fall behavior of planar snow crystals, conical graupel and small hail, *J. Atmos. Sci.*, **28**, 110–115.
- Locatelli, J. D., and P. V. Hobbs (1974), Fall speeds and masses of solid precipitation particles, *J. Geophys. Res.*, **79**, 2185–2197.
- Magono, C., and T. Nakamura (1995), Aerodynamic studies of falling snowflakes, *J. Meteorol. Soc. Jpn.*, **43**, 139–147.
- Matrosov, S. Y. (1998), A dual-wavelength radar method to measure snowfall rate, *J. Appl. Meteorol.*, **37**, 1510–1521.
- Matrosov, S. Y. (2007), Modeling backscatter properties of snowfall at millimeter wavelengths, *J. Atmos. Sci.*, **64**, 1727–1736.
- Mitchell, D. L. (1996), Use of mass- and area-dimensional power laws for determining precipitation particle terminal velocities, *J. Atmos. Sci.*, **53**, 1710–1723.
- Mitchell, D. L., and A. J. Heymsfield (2005), Refinements in the treatment of ice particle terminal velocities, highlighting aggregates, *J. Atmos. Sci.*, **62**, 1637–1644.
- Mitchell, D. L., R. Zhang, and R. L. Pitter (1990), Mass-dimension relationships for ice particles and the influence of riming on snowfall rates, *J. Appl. Meteorol.*, **29**, 153–163.
- Mory, M. (2011), *Fluid Mechanics for Chemical Engineering*, 422 pp., ISTE Ltd., London.
- Nakaya, U., and T. Terada, Jr. (1935), Simultaneous observations of the mass, falling velocity and form of individual snow crystals, *J. Fac. Sci. Hokkaido Imp. Univ., Ser. II*, **1**, 191–200.
- Newman, A. J., P. A. Kucera, and L. F. Bliven (2009), Presenting the Snowflake Video Imager (SVI), *J. Atmos. Oceanic Technol.*, **26**, 167–179.
- Petersen, W. A., T. L'Ecuier, and D. Moisseev (2011), The NASA CloudSat/GPM Light Precipitation Validation Experiment (LPVEx), *The Earth Observer*, **23**(4–8), 21.
- Rodgers, C. (2000), *Inverse Methods for Atmospheric Sounding*, 240 pp., World Scientific, Singapore.
- Shannon, C. E., and W. Weaver (1949), *The Mathematical Theory of Communication*, 117 pp., Univ. of Illinois Press, Urbana, Ill.
- Sheppard, B. E., and P. I. Joe (2008), Performance of the precipitation occurrence sensor system as a precipitation gauge, *J. Atmos. Oceanic Technol.*, **25**, 196–212.
- Skofronick-Jackson, G. M., M.-J. Kim, J. A. Weinman, and D.-E. Chang (2004), A physical model to determine snowfall over land by microwave radiometry, *IEEE Trans. Geosci. Remote Sens.*, **42**, 1047–1058.

- Sutherland, W. (1893), The viscosity of gases and molecular force, *Philos. Mag., Ser., 5*(36), 507–531.
- Thurai, M., and V. N. Bringi (2005), Drop axis ratios from a 2D video disdrometer, *J. Atmos. Sci.*, *22*, 966–978.
- Vaisala, O. (2002), Weather sensor FD12P user's guide M210296en-A, Vaisala Oyj, Helsinki, 154 pp. [Available from <http://www.vaisala.com/en/services/technicalsupport/downloads/Pages/User-Manuals.aspx>, accessed 4 August, 2013.]
- Warren, S. G. (1984), Optical constants of ice from the ultraviolet to the microwave, *Appl. Opt.*, *23*, 1206–1225.
- Wood, N. B. (2011), Estimation of snow microphysical properties with application to millimeter-wavelength radar retrievals for snowfall rate, PhD dissertation, Colorado State Univ., Fort Collins, Colo. [Available from Colorado State University, Digital Collections, <http://hdl.handle.net/10217/48170>.]
- Wood, N. B., T. S. L'Ecuyer, F. L. Bliven, and G. L. Stephens (2013), Characterization of disdrometer uncertainties and impacts on estimates of snowfall rate and radar reflectivity, *Atmos. Meas. Tech.*, *6*, 3635–3648, doi:10.5194/amt-6-3635-2013.
- Zikmunda, J., and G. Vali (1972), Fall patterns and fall velocities of rimed ice crystals, *J. Atmos. Sci.*, *29*, 1334–1347.
- Zikmunda, J., and G. Vali (1977), Corrigendum, *J. Atmos. Sci.*, *34*, 1675.